ADVANCED ENERGY MATERIALS
www.advenergymat.de

Sodium Plating from Na-β″-Alumina Ceramics at Room Temperature, Paving the Way for Fast-Charging All-Solid-State Batteries

*Marie-Claude Bay, Michael Wang, Rabeb Grissa, Meike V. F. Heinz, Jeff Sakamoto, and Corsin Battaglia**

All-solid-state batteries with an alkali metal anode have the potential to achieve high energy density. However, the onset of dendrite formation limits the maximum plating current density across the solid electrolyte and prevents fast charging. It is shown that the maximum plating current density is related to the interfacial resistance between the solid electrolyte and the metal anode. Due to their high ionic conductivity, low electronic conductivity, and stability against sodium metal, Na-β″-alumina ceramics are excellent candidates as electrolytes for room-temperature all-solid-state batteries. Here, it is demonstrated that a heat treatment of Na-β″-alumina ceramics in argon atmosphere enables an interfacial resistance <10 Ω cm^2 and current densities up to 12 mA cm^{-2} at room temperature. The current density obtained for Na-β″-alumina is ten times higher than that measured on a garnet-type $Li_7La_3Zr_2O_{12}$ electrolyte under equivalent conditions. X-ray photoelectron spectroscopy shows that eliminating hydroxyl groups and carbon contaminations at the interface between Na-β″-alumina and sodium metal is key to reach such values. By comparing the temperature-dependent stripping/plating behavior of Na-β″-alumina and $Li_7La_3Zr_2O_{12}$, the role of the alkali metal in governing interface kinetics is discussed. This study provides new insights into dendrite formation and paves the way for fast-charging all-solid-state batteries.

1. Introduction

Enabling reversible stripping and plating of alkali metals at current densities >10 mA cm^{-2} at room temperature is key for enabling next-generation batteries with an energy and power density surpassing that of established battery technologies. However, repeated cycling of a lithium metal anode in a liquid electrolyte leads to the formation of lithium metal dendrites that short-circuit the cell and constitute a serious safety hazard.[1] A similar phenomenon is observed in solid electrolytes employed in all-solid-state batteries, where lithium metal tends to deposit inside the electrolyte upon repeated cycling resulting ultimately in a short-circuit between anode and cathode.[2–5]

While the underlying mechanisms are still under debate, it was shown that the critical current density (CCD) for dendrite formation is related to the interfacial resistance between solid electrolyte and the metal anode.[6] Several strategies have been adopted to reduce the interfacial resistance, e.g., at the interface between a $Li_7La_3Zr_2O_{12}$ (LLZO) electrolyte and a lithium metal anode. LLZO is currently investigated intensively because of its high ionic conductivity (≈1 mS cm^{-1} at room temperature) and high stability toward lithium metal.[7,8] Strategies include the use of interfacial layers (e.g., Au,[9] Ge[10]), heat treatments (HTs) to remove surface contamination from the electrolyte,[6] or promoting contact by pressurizing the cell during cycling.[11,12] Despite obtaining interfacial resistances comparable to values measured for the

M.-C. Bay, Dr. R. Grissa, Dr. M. V. F. Heinz, Dr. C. Battaglia
Empa
Swiss Federal Laboratories for Materials Science and Technology
Überlandstrasse 129, 8600 Dübendorf, Switzerland
E-mail: Corsin.Battaglia@empa.ch

The ORCID identification number(s) for the author(s) of this article can be found under https://doi.org/10.1002/aenm.201902899.

© 2019 The Authors. Published by WILEY-VCH Verlag GmbH & Co. KGaA, Weinheim. This is an open access article under the terms of the Creative Commons Attribution-NonCommercial-NoDerivs License, which permits use and distribution in any medium, provided the original work is properly cited, the use is non-commercial and no modifications or adaptations are made.

DOI: 10.1002/aenm.201902899

M.-C. Bay
Institute for Environment and Natural Resources
Crystallography
Albert-Ludwigs-University Freiburg
79098 Freiburg im Breisgau, Germany

M. Wang, Prof. J. Sakamoto
Department of Materials Science & Engineering
University of Michigan
Ann Arbor, MI 48109, USA

Prof. J. Sakamoto
Department of Mechanical Engineering
University of Michigan
Ann Arbor, MI 48109, USA

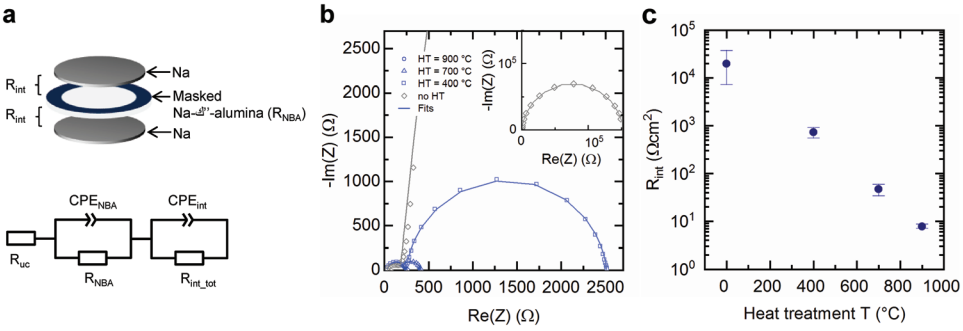


Figure 1. Impact of heat-treatment (HT) temperature on interfacial resistance at room temperature. a) Schematic of the symmetric Na/Na-β''-alumina/Na cell and equivalent circuit for fitting the impedance spectra. b) Representative Nyquist plots for the different heat-treatment temperatures. Markers represent experimental data and lines represent the fitted data. c) Interfacial resistance as a function of heat-treatment temperature.

interface between a liquid electrolyte and lithium metal, CCD values remain far below fast charging requirements (e.g., 10 mA cm^{-2} corresponding to an areal charge capacity of 5 mAh cm^{-2} charged/discharged at 2C[13]).

In this study, we investigate Na-β''-alumina ceramics as electrolyte candidate for fast-charging all-solid-state batteries. Owing to its high ionic conductivity, low electronic conductivity, and stability against sodium metal, Na-β''-alumina is already commercially employed in high-temperature sodium–nickel-chloride (NaNiCl) and sodium–sulfur (NaS) batteries operating near 300 °C.[14–16] However, high interfacial resistance, possibly associated with poor sodium wetting and the presence of surface impurities, has impeded its use as solid electrolyte for room-temperature batteries.[16,17]

Here, we show that by applying a heat treatment in argon atmosphere to a finely polished Na-β''-alumina surface, a low interfacial resistance to sodium metal <10 Ω cm^2 can be achieved, enabling CCD values of 12 mA cm^{-2} at room temperature fulfilling fast charging requirements. We also investigate the dependence of the CCD values on the total charge transferred. Compared to LLZO, we observe a tenfold increase in current density despite similar transference numbers. We are also discussing the critical role of the electronic conductivity of the electrolyte and the melting temperature of the alkali metal on the CCD.

2. Results and Discussion

2.1. Impact of Heat-Treatment Temperature on Interfacial Resistance and Interface Chemistry

To study the impact of a heat treatment on the interfacial resistance (R_{int}) between sodium metal and Na-β''-alumina, potentiostatic electrochemical impedance spectroscopy (PEIS) measurements were conducted on Na-β''-alumina pellets heat treated in argon at temperatures between 400 and 900 °C and compared to as-polished untreated samples. These measurements were performed on symmetric Na/Na-β''-alumina/Na cells as depicted in **Figure 1**a. A mask was applied on Na-β''-alumina to obtain a well-defined contact area between Na-β''-alumina and the Na disc and a pressure of 3.4 MPa was applied during PEIS measurements. Representative Nyquist plots for the various heat-treatment conditions are shown in Figure 1b. The PEIS spectra reveal two semicircles representing the impedance contributions from the Na-β''-alumina ceramic characterized by an apex frequency of 4.3×10^5 Hz and from the Na/Na-β''-alumina interface characterized by an apex frequency ranging from 10 to 400 Hz. While the Na-β''-alumina contribution remains constant, the interface contribution is drastically reduced with increasing heat-treatment temperature. To quantify the change in interfacial resistance with the heat-treatment temperature, the PEIS spectra were fitted with two parallel R/CPE circuits in series together with an additional resistance (R_{uc}) to account for any uncompensated resistances, e.g., from the cell casing and electrical connections (Figure 1a). The interfacial resistances were normalized by the mask area and divided by two because of the two interfaces measured. The results of the fits are presented in **Table 1** and in Figure 1c in a semilogarithmic scale as a function of the heat-treatment temperature. A significant decrease of the interfacial resistance from tens of thousands of Ω cm^2 for nonheat-treated samples to 8 Ω cm^2 is achieved by heat treating the Na-β''-alumina pellets at 900 °C, while the CPE values increases by two orders of magnitude. Heat treating Na-β''-alumina ceramics in argon atmosphere represents thus a very effective method to reduce the interfacial resistance to sodium metal.

To investigate the effect of the heat treatment on the Na-β''-alumina electrolyte surface, we performed X-ray photoelectron spectroscopy (XPS) on Na-β''-alumina pellets before and after heat treatment at 400, 700, and 900 °C. Spectra of the C 1s, O 1s, Al 2p, and Na 2s core levels are shown in **Figure 2**. The detailed XPS data fitting procedure is described in Section A in the Supporting Information and results are summarized in Figure 2m and Table S1 in the Supporting Information. The

Table 1. Fitting results of room temperature interfacial resistance (R_{int}) and capacitance (CPE_{int}) for the various heat-treatment (HT) conditions.

HT [°C]	R_{int} [Ω cm^2]	CPE_{int} [F s^{a-1}]
None	19 909	2.7×10^{-7}
400	735	4.1×10^{-7}
700	47	1.4×10^{-6}
900	8	1.8×10^{-5}

© 2019 The Authors. Published by WILEY-VCH Verlag GmbH & Co. KGaA, Weinheim

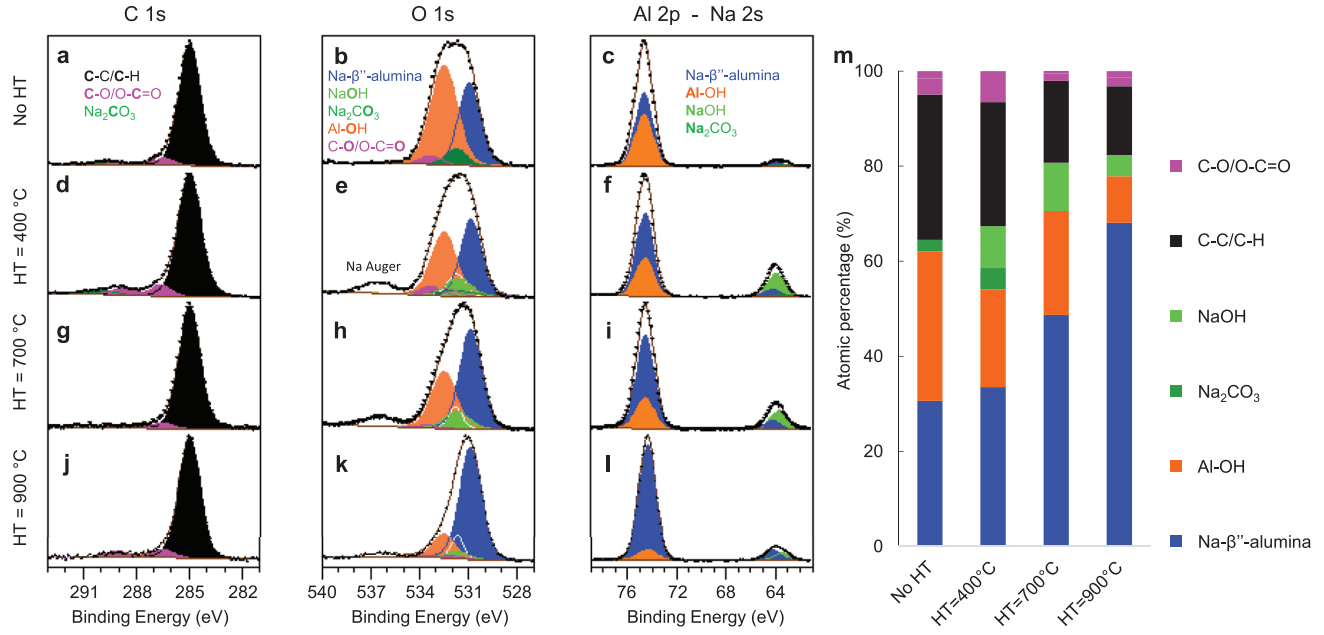


Figure 2. XPS analysis of Na-β''-alumina surfaces before and after heat treatment. XPS spectra of C 1s, O 1s, and Al 2p–Na 2s core levels of the Na-β''-alumina a–c) before heat treatment, and after heat treatment under argon atmosphere d–f) at 400 °C, g–i) at 700 °C, and at j–l) 900 °C, respectively. m) Summary of surface chemical composition, estimated by XPS, for all Na-β''-alumina samples.

main peak in the C 1s spectra at 285.0 eV (by calibration) is attributed to adventitious carbon species (C—C/C—H). Oxidized carbon contamination (C—O and O—C=O) is detected at higher binding energies. Only a very small amount of Na_2CO_3 (<5 at%) is detected at the surface above 289.9 eV before and after heat treatment at 400 °C and is no longer detected after heat treatment at higher temperatures (Figure S1, Supporting Information).

The O 1s peak for the nontreated Na-β''-alumina is very broad and cannot be fitted with a single component. The width of this peak reduces significantly with increasing heat-treatment temperature accompanied by the formation of a small shoulder on the high binding energy side. Following ref. [18], we choose to take two main components to fit this peak representing oxygen (Al–O, ≈530.9 eV, blue color in Figure 2) in the crystal structure and hydroxyl (Al–OH, 532.5 eV, orange color in Figure 2) groups present at the surface. In addition, oxygen atoms bound to carbon (C—O, O—C=O, Na_2CO_3) are taken into account in the ratio determined from the C 1s peak, corrected for their respective photoelectron cross sections (Table S2, Supporting Information) and chemical formula. Interestingly, while the Al–OH component is comparable in area to the Al–O component, it reduces significantly after heat treatment at 900 °C. This is strong evidence that reducing the amount of hydroxyl groups at the interface is key to obtain low ionic interfacial resistance to sodium metal.

For completeness, we also show the Al 2p and Na 2s spectra. Following refs. [18,19], we refrain from deconvoluting the Al 2p doublet ($2p_{3/2}$ and $2p_{1/2}$) into an Al–O and Al–OH component with different binding energies. Instead, both components are constrained to the same binding energy and the peak area ratio between the two components is constrained to the value calculated from the analysis of the O 1s peak. Note that the presence of the Al 2p peak confirms that the surface contamination layer is thinner than the photoelectron inelastic mean free path.[20] From the Na 2s peak, we observe the presence of NaOH, for the heat-treated samples only, which we ascribe to segregated sodium reacting to NaOH at the surface during the short transfer into the XPS chamber. We confirmed experimentally that this short air exposure does not affect the interfacial resistance between sodium metal and Na-β''-alumina.

XPS results are summarized in Figure 2m showing that the heat treatment results in a significant reduction of hydroxyl groups and carbon contaminations at the Na-β''-alumina surface.

2.2. Temperature-Dependent Transport Properties

In order to better understand the transport kinetics at the Na/Na-β''-alumina interface, we analyze the different conduction processes as a function of temperature on samples heat treated at 900 °C. **Figure 3**a exemplarily shows Nyquist plots of Na/Na-β''-alumina/Na cells measured from 0 to 60 °C. Enlarged graphs for all temperatures can be found in Figure S3 in the Supporting Information. To avoid hysteresis effects due to thermal cycling, each measurement was taken with a freshly and identically prepared cell. It is clear that the impedance of both the Na-β''-alumina ceramic and the interface decrease as the temperature increases. Extracting both contributions using the equivalent circuit of Figure 1a results in the temperature-dependent ion conductivity and interfacial resistance shown in Figure 3b. The ionic conductivity of the Na-β''-alumina ceramic at room temperature is 1.6 mS cm^{-1} and follows an Arrhenius behavior with activation energy of 0.41 ± 0.02 eV derived

© 2019 The Authors. Published by WILEY-VCH Verlag GmbH & Co. KGaA, Weinheim

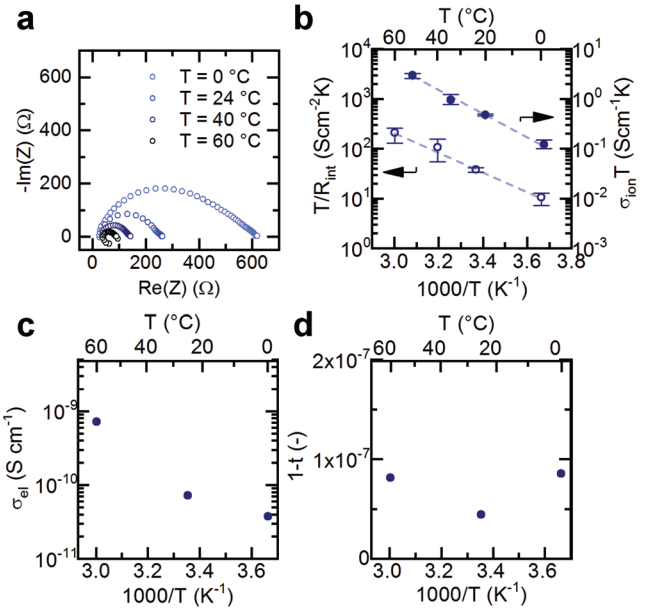


Figure 3. a) Representative Nyquist plots as a function of temperature on samples heat treated at 900 °C. Temperature-dependent b) interfacial resistance and ionic conductivity, c) electronic conductivity, and d) ionic transference number t plotted as $1 - t$ for readability.

from a linear fit of $\ln(\sigma_{ion}T)$ versus $1000/T$. In comparison, the interfacial process follows an Arrhenius behavior with similar activation energy of 0.40 ± 0.03 eV derived from a linear fit of $\ln(T/R_{int})$ versus $1000/T$. An analogous situation was recently also reported for the Li/LLZO interface and was interpreted as pointing toward an interfacial resistance dominated by current constriction resulting from void formation at the interface upon stripping.[11] As pressure is applied during the measurements, a good contact is expected to be maintained also at low temperatures. Therefore, we attribute the temperature-dependent interfacial resistance to improved kinetics rather than to a change in viscosity of sodium metal with temperature. Additional requirements for solid electrolytes are low electronic conductivity σ_{el} and high ionic transference number t. Figure 3c,d shows the electronic conductivity and ionic transference number t from 0 to 60 °C, plotted as $1 - t$ for better readability. At room temperature, a low electronic conductivity of 7×10^{-11} S cm^{-1} is measured, which increases only slightly with temperature following an Arrhenius behavior with an activation energy of 0.42 eV. Corresponding transference numbers are close to 1 in this temperature range. Overall, the high ionic conductivity coupled to low electronic conductivity of Na-β''-alumina ceramics and interfacial charge transfer process with low resistivity are key enablers for the development of solid-state Na/Na-β''-alumina batteries.

2.3. Critical Current Densities in Na-β''-Alumina Ceramics as Function of Charge and R_{int}

After demonstrating low interfacial resistance and favorable charge transport properties, we now focus on the sodium stripping/plating behavior in symmetric Na/Na-β''-alumina/Na cells. The CCDs at which dendrites propagate through Na-β''-alumina ceramics were determined by galvanostatic measurements. In order to ensure a good contact between sodium metal and Na-β''-alumina ceramics, 10 cycles of 1 h at a current density of 10 μA cm^{-2} were first applied.[21] CCD measurements were then performed with increasing current density at each cycle, while transferring a constant charge density of 0.25 mAh cm^{-2} to allow direct comparison with results from a recent studies on LLZO.[22] To mitigate too strong contact loss during stripping as recently demonstrated in lithium metal in contact with LLZO,[11,12] the cells were put under pressure at 3.4 MPa. After the measurement, the pressure was recorded to be still about −5% of the initial value. The potential response during a typical CCD measurement is shown in **Figure 4**a for a sample heat treated at 900 °C. Additional CCD experiments are shown in Figures S4 and S5 in the Supporting Information. In the example in Figure 4a, the CCD was reached at 9 mA cm^{-2} as observed by a sudden drop of the potential to 0 V (see arrow in Figure 4e), indicating a short-circuit in the cell due to dendrite formation. In some cases, if the dendrites short the cells only locally at point contacts, the potential may partially recover as shown in the example of Figure 4e. To confirm the short in the cell, PEIS was performed between each stripping/plating cycle. Figure 4b shows typical PEIS spectra before and after the CCD was reached. Below the CCD, the spectra are dominated by the electrolyte contribution (as described by parallel connection of R_{NBA} and CPE_{NBA} in Figure 1a). After short-circuiting, the electrolyte contribution is significantly reduced, and the spectra are dominated by a resistive behavior, with some minor capacitance contributions, possibly related to the local point contact of the sodium dendrite. A closer look on the potential response at different stages of the measurement (boxes in Figure 4a), are shown in Figure 4c–e. At low current densities, the potential response follows an Ohmic behavior, $U = RI$, where U is the potential, R is the total cell resistance, and I is the current as observed by the stable potential. Due to negligible interfacial resistance, the overpotential at low current density is given by the electrolyte only. As the current density increases, the potential response deviates from Ohmic behavior until CCD is reached. Such an increase of potential was recently ascribed to void formation in lithium metal at the interface to LLZO during stripping,[12] but measurements with a reference electrode would be required to decouple stripping from plating effects.

We now explore the impact of the charge density and interfacial resistance on CCD. **Figure 5**a,b compares the potential response of cells cycled with charge densities of 0.25 and 3 mAh cm^{-2}, respectively, up to a current density of 6.6 mA cm^{-2} using Na-β''-alumina pellets heat treated at 900 °C. While the cell cycled at a charge density of 0.25 mAh cm^{-2} does not fail up to 6.6 mA cm^{-2}, the cell cycled at a charge of 3 mAh cm^{-2} fails at 5.5 mA cm^{-2} as observed by the sudden drop in potential response to 0 V, indicated by the arrow in Figure 5b. Compared to the potential response of the cell cycled at low charge density, the polarization of the cell cycled at high charge density increases continuously with increasing current density until the cut-off voltage of 4.5 V is reached (axis cut at 1 V for better readability). Early cell failure with increased charge supports the void formation hypothesis. When a larger amount of charge is transferred per cycle, void

© 2019 The Authors. Published by WILEY-VCH Verlag GmbH & Co. KGaA, Weinheim

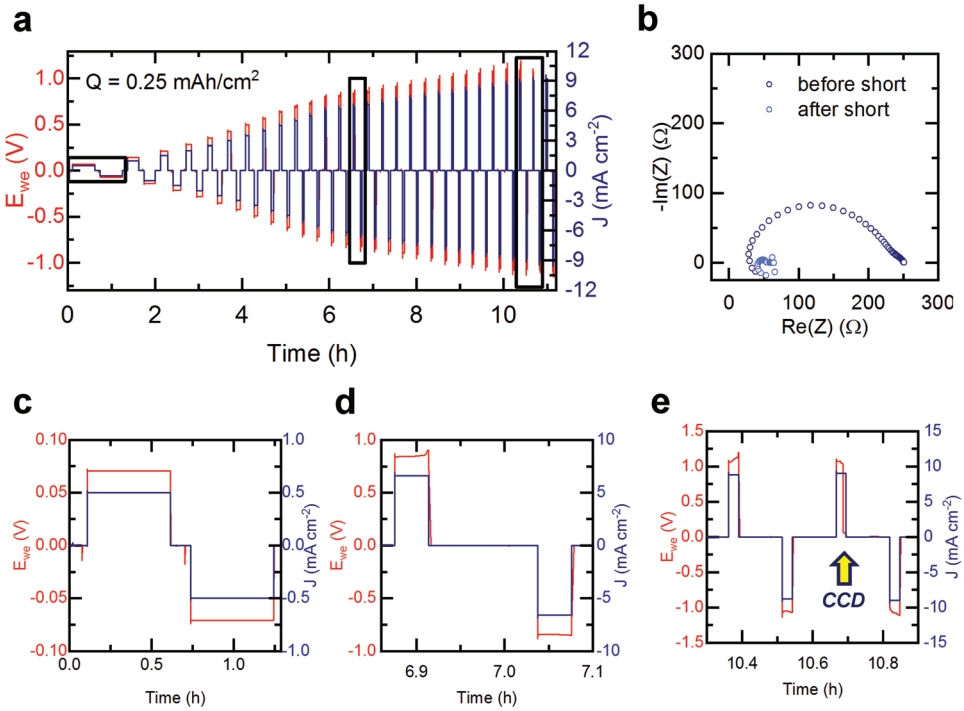


Figure 4. a) Representative potential response of a Na/Na-β''-alumina/Na cell undergoing CCD measurement at room temperature and charge of 0.25 mAh cm^{-2} per half cycle. b) Nyquist plots before and after short-circuit. Closer view on the potential response during CCD measurement c) at low current densities d) at medium current densities, and e) close to short-circuit, showing an increase of the polarization. Additional CCD experiments are shown in Figures S4 and S5 in the Supporting Information.

formation in sodium metal near the interface to Na-β''-alumina reduces the contact surface area and thus increases the interfacial resistance and the local current densities at the remaining contact spots. As a result, higher overpotentials are needed to supply a constant current. While void formation can be avoided by increasing the pressure,[11,12] we performed all CCD measurements with a charge density of 0.25 mAh cm^{-2} to enable direct comparison with CCD values on LLZO.[22]

The impact of increasing HT temperature is shown in Figure 5c. The CCD values increase significantly with decreasing interfacial resistance. For the maximum heat-treatment temperature applied, an average CCD value over four samples of 12 mA cm^{-2} is obtained. To the best of our knowledge, this is the highest reported CCD value for a solid electrolyte at room temperature (without implementation of a porous electrolyte layer that locally reduces the current density by increasing the surface area as in ref. [23]). Increasing CCD values with decreasing interfacial resistance have previously been reported for LLZO,[6] where this effect was attributed to the suppression of localized regions featuring higher current densities, often referred to as "hot spots." Similar observations were also made for Na-β''-alumina at elevated temperatures using a molten sodium metal anode, where higher charge could be passed in cells featuring lower charge transfer resistances.[24] Note that the maximum heat-treatment temperature in this study was limited by the furnace to 900 °C. While it is possible that higher temperatures may further decrease the interfacial resistance and thus increase the CCD value, void formation at the interface may limit the physical maximum CCD. Nonetheless, this surface treatment gives optimistic results for the implementation of fast-charging all-solid-state batteries.

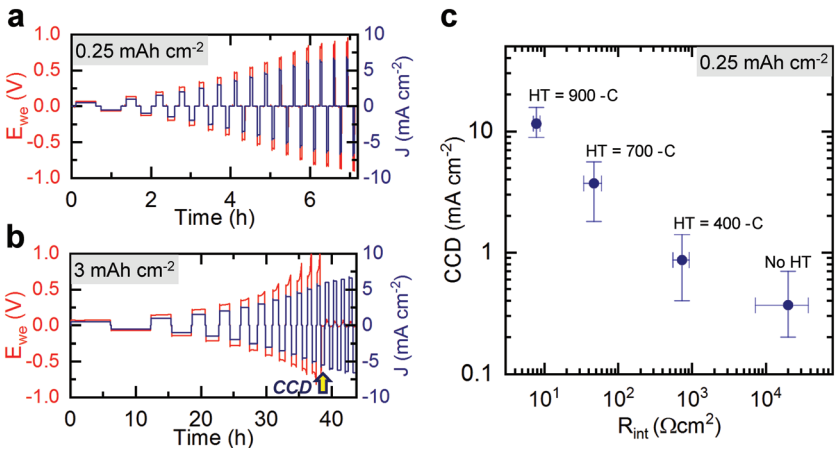


Figure 5. Representative potential responses of Na/Na-β''-alumina/Na cells undergoing CCD measurements at total transferred charge Q per half cycle of a) Q = 0.25 mAh cm^{-2} and b) Q = 3 mAh cm^{-2} for Na-β''-alumina samples heat treated at 900 °C (while the potential response of the two last cycles before failure reached a limit of 4.5 V, the maximum value of the y-axis scale bar is 1 V for better readability). c) CCD as a function of interfacial resistance.

© 2019 The Authors. Published by WILEY-VCH Verlag GmbH & Co. KGaA, Weinheim

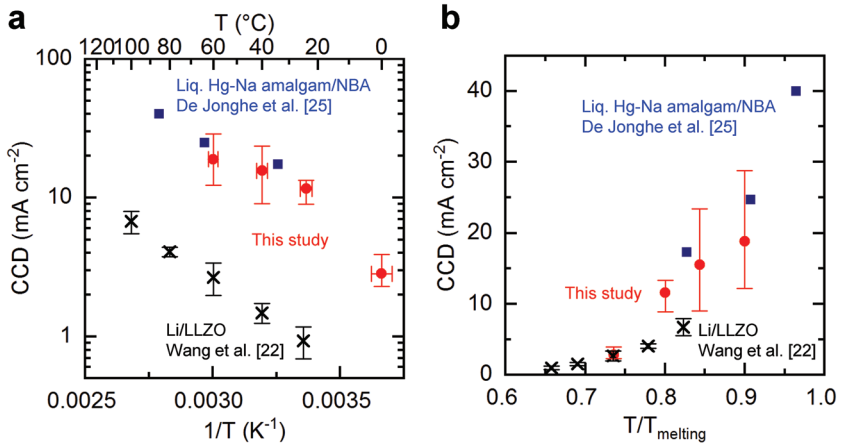


Figure 6. Temperature-dependent CCD and comparison with literature a) in Arrhenius representation b) as a function of homologous temperature ($T/T_{melting}$).

2.4. Temperature-Dependent CCD and Comparison with Literature

The effect of stripping/plating temperature on the CCD was investigated on samples heat treated at 900 °C in a temperature range from 0 to 60 °C. The results are plotted in **Figure 6**a in Arrhenius representation. Similarly to literature,[25,22] we find an exponential relationship between CCD and inverse temperature (taking into account the error bars) with activation energy of 0.27 eV. By increasing the temperature to 60 °C, critical current densities up to 19 mA cm^{-2} can be achieved, which is in agreement with acoustic measurements from the 1980s employing a liquid mercury sodium amalgam.[25] While this temperature behavior is currently not completely understood, Han et al. recently proposed that dendrite formation is governed by the electronic conductivity of the electrolyte, governing the rate at which sodium ions are reduced to metallic sodium in the bulk of the solid electrolyte above the plating potential.[26] They concluded that the electronic conductivity should be lower than 10^{-12} S cm^{-1} to enable dendrite-free plating at 10 mA cm^{-2}. Although this criterion corresponds roughly to the measured values at room temperature in this study (7×10^{-11} S cm^{-1}, 12 mA cm^{-2}), the electronic conductivity at 60 °C deviates by almost three orders of magnitude (7×10^{-10} S cm^{-1}) from this threshold, whereas the critical current densities improves by 30%. Furthermore, it was also shown that Na-β''-alumina can sustain critical current densities up to 300 mA cm^{-2}[25] at 350 °C at an electronic conductivity of ≈10^{-8} S cm^{-1}.[27] It is clear that the ionic conductivity and charge transfer kinetics are also improved at the same time, and therefore a theory only based on the electronic conductivity cannot fully explain the temperature-dependent CCD measurements. Some of us recently hypothesized that the properties of the alkali metal electrode may govern dendrite formation.[22] It was reported that flux imbalances at the interface caused by differences between the metal self-diffusivity in the alkali metal and the ionic diffusivity in the electrolyte may create metal pile-up at the interface, which eventually acts as nucleation site for dendritic growth. To better understand the role of the electrode metal, we compare in Figure 6a the results for LLZO obtained in a previous study.[22] Note that identical measurement conditions were applied and similar interfacial resistances were obtained. Over the measured temperature range, the CCD values for Na-β''-alumina are systematically ten times higher than for LLZO. It is interesting to note that the error bars for Na-β''-alumina are also larger. On the one hand, this could be the result of the bimodal grain and pore size distribution of the Na-β''-alumina ceramics (Figure S6, Supporting Information) as recently described in detail in a previous publication.[28] In particular, pores at the interface may lead to an increase in local current density. On the other hand, this could be the result of an amplification effect of surface inhomogeneities at higher current densities, as also observed to a smaller extent for LLZO for increasing temperature. When comparing the behavior of the two alkali metals, we should also take into account their different melting temperatures (97.79 °C for Na, 180.5 °C for Li) as they differ in viscosity for the same measurement temperature. In Figure 6b, we plot the CCD values as a function of the homologous temperature, defined as the (absolute) temperature (T) divided by the melting temperature ($T_{melting}$) of the alkali metal. While similar CCD values are obtained for both the Na and the Li system at, e.g., at $T/T_{melting}$ of 0.74, those of the Na system feature a much stronger exponential increase above a homologous temperature of 0.8 (corresponding to >24 °C for Na system, >90 °C for Li system). To better understand these results, we compare in Figure S7 in the Supporting Information temperature-dependent diffusivities in both the Li and the Na systems as reported in literature[29,30] and estimated the diffusivities of Li^+ in LLZO and Na^+ in Na-β''-alumina applying Nernst–Einstein equation.[22] In the lithium system, the diffusivities of Li^0 in Li and Li^+ in LLZO differ by a factor ≈100 (5×10^{-11} vs 2×10^{-9} cm^2 s^{-1} at room temperature, respectively). In comparison, the diffusivities of Na^0 in Na and Na^+ in Na-β''-alumina differ by a factor of only ≈10 (5×10^{-9} vs 3×10^{-8} cm^2 s^{-1} at room temperature, respectively). Furthermore, it is interesting to note that the self-diffusivity of sodium is about hundred times the self-diffusivity of lithium (5×10^{-9} vs 5×10^{-11} cm^2 s^{-1} at room temperature, respectively). Interestingly, the Li^+ diffusivity in LiPON (2×10^{-8} cm^2 s^{-1}[31]) was reported to be on the same order of magnitude as the Na^+ diffusivity in Na-β''-alumina. In addition, thin-film all-solid-state batteries based on LiPON with areal capacities up to 160 µAh cm^{-2} were cycled up to 10 mA cm^{-2} without dendrite formation.[32] Thus, while diffusivity may play a role in governing flux balance between the alkali metal and solid-state electrolyte, it should be acknowledged that other parameters such as the mechanical properties of the anode can affect interface stability.

3. Conclusion

Applying a heat treatment on finely polished Na-β''-alumina ceramics in argon atmosphere to eliminate surface hydroxyl groups and carbon contaminations, the interfacial resistance of

© 2019 The Authors. Published by WILEY-VCH Verlag GmbH & Co. KGaA, Weinheim

symmetric Na/Na-β''-alumina cells was reduced from hundreds of Ω cm^2 to 8 Ω cm^2 at room temperature. This improvement in interfacial resistance drastically increases the critical current density from 0.3 to 12 mA cm^{-2} for a total transferred charge density of 0.25 mAh cm^{-2} per half cycle. Increasing the charge density was demonstrated to increase the cell polarization, presumably due to the formation of voids at the interface between electrolyte and metal anode, highlighting the need of applying stack pressure. Compared to the garnet-type LLZO, the critical current densities obtained for Na-β''-alumina, measured on the same setup under identical measurements conditions,[22] are ten times higher despite similar transference number. While the temperature-dependent critical current density measurements both show an exponential behavior with comparable activation energy, we attribute the tenfold difference in CCD to the diffusive and mechanical properties of the alkali metal and of the solid electrolyte.

Currently the development of all-solid-state batteries based on sodium metal anodes is hindered by the lack of availability of an appropriate sodium cathode material that can compete in performance, e.g., with nickel-rich layered oxides employed in lithium-ion batteries (e.g., NMC811). However, our results demonstrate that if such a cathode material becomes available in the near future, an all-solid-state sodium metal battery with fast charging capabilities based on a Na-β''-alumina electrolyte becomes a very promising option for rapid commercialization and market deployment.

4. Experimental Section

Spray-dried Li-stabilized Na-β''-alumina powders were prepared by solid-state synthesis from boehmite (AlO(OH)), lithium hydroxide (LiOH), and sodium carbonate (Na_2CO_3).[28] Powders were pressed into green bodies of 15.5 mm diameter. These were sintered for 5 min at 1600 °C in static air in a high-temperature laboratory furnace (Carbolite Gero HTF 1700) applying constant heating and cooling rates of 3 °C min^{-1}. To mitigate sodium (and lithium) loss and to facilitate shrinkage during sintering, samples were placed on green buffer discs made from the same Na-β''-alumina powder. Samples and buffer discs were encapsulated within a dense magnesium-spinel dome and a corresponding magnesium-spinel support disc with a constant ratio of Na-β''-alumina mass (samples plus buffer disc) to encapsulated volume of 0.14 g cm^{-3}. Pellets of relative density of 97.6 ± 0.1% were obtained. The pellets were then ground plan-parallel with increasingly finer sandpapers and polished with a succession of diamond pastes to a final polish using 0.1 µm diamond paste. Scanning electron microscopy analysis revealed homogeneous grain size distribution in the micrometer range and a bimodal pore size distribution with coarse pores of tens of micrometer diameter and small pores in the sub-micrometer range (see SEM images in Figure S6 in the Supporting Information). A detailed compositional and microstructural study was reported.[28] The resulting pellets had final dimensions of 1.4 ± 0.3 mm thickness and 12.7 mm diameter. The samples were then heat treated in argon atmosphere for 3 h at temperatures between 400 and 900 °C.

Cell assembly and electrochemical characterization were performed under argon atmosphere in a glovebox. The heat-treated Na-β''-alumina ceramics were first masked on both sides to an area of 0.49 cm^2 using polyimide foil. Mechanically cleaned sodium foils were then pressed onto both sides of the masked pellets at a pressure of 3.4 MPa. Electrochemical characterization was performed using a Biologic VMP-300 galvanostat/potentiostat using nickel current collectors at a pressure of 3.4 MPa in an argon glovebox. The temperature-dependent ion-conductivity of Na-β''-alumina was extracted from PEIS data measured at frequencies between 0.5 Hz and 7 MHz with a 20 mV sinusoidal amplitude. Measurements at frequencies >1 MHz were not taken into account for the fitting. The temperature-dependent electronic conductivity was determined by a DC polarization method (Mott–Schottky) at 0.2 V versus Na/Na$^+$ after 12 h stabilization (1 V was applied for the measurement at 0 °C due to resolution limits) using a sputtered Ni working electrode and a Na counter electrode. The assessment of the CCD was performed by galvanostatic measurements applying an initial pressure of 3.4 MPa. The current density was increased at each cycle while transferring a constant charge of 0.25 or 3 mAh cm^{-2}. PEIS was conducted before and after each plating and stripping cycle. CCD was defined as the current density when short-circuit of the cell occurred, indicated by a sudden drop in potential response and cell impedance. CCD values were given as the average over 3 to 4 measurements and the error bars represented the maximum and minimum values.

XPS measurements were performed at room temperature on a PHI Quantum 2000 using a monochromated Al Kα X-ray source (1486.6 eV) with a pass energy of 30 eV. All measurements were conducted on three different areas, 150 µm in diameter, of each sample. Sample charging was prevented by charge compensation provided by a low energy electron and an argon ion gun. XPS data were processed with the CasaXPS software. Spectra were calibrated by setting the hydrocarbon component of the C 1s photoemission peak to 285.0 eV binding energy.

Supporting Information

Supporting Information is available from the Wiley Online Library or from the author.

Acknowledgements

M.-C.B. and M.W. contributed equally to this work. M.-C.B., R.G., M.V.F.H., and C.B. obtained funding by InnoSuisse under contract number 18126.1 PFEN-IW. These authors also acknowledge support by InnoSuisse through funding for the Swiss Competence Center for Energy Research (SCCER) Heat and Electricity Storage under contract number 1155-002545. M.W. and J.S. would like to acknowledge funding support from the U.S. Department of Energy ARPA-E DE-AR0000653. All authors acknowledge the support of Empa's Nanoscale Materials Science Laboratory for access to XPS and are grateful to Francesco Pagani for the nickel sputtering and to Ryo Asakura for useful discussions on the electronic conductivity measurements.

Conflict of Interest

The authors declare no conflict of interest.

Keywords

all-solid-state batteries, critical current density, dendrites, fast charging, Na-β''-alumina electrolyte, sodium metal anodes, surface treatment

Received: September 4, 2019
Revised: October 19, 2019
Published online: December 4, 2019

[1] D. Lin, Y. Liu, Y. Cui, *Nat. Nanotechnol.* **2017**, *12*, 194.
[2] Y. Ren, Y. Shen, Y. Lin, C.-W. Nan, *Electrochem. Commun.* **2015**, *57*, 27.
[3] E. J. Cheng, A. Sharafi, J. Sakamoto, *Electrochim. Acta* **2017**, *223*, 85.

© 2019 The Authors. Published by WILEY-VCH Verlag GmbH & Co. KGaA, Weinheim

[4] L. Porz, T. Swamy, B. W. Sheldon, D. Rettenwander, T. Frömling, H. L. Thaman, S. Berendts, R. Uecker, W. C. Carter, Y.-M. Chiang, *Adv. Energy Mater.* **2017**, *7*, 1701003.
[5] A. Gupta, E. Kazyak, N. Craig, J. Christensen, N. P. Dasgupta, J. Sakamoto, *J. Electrochem. Soc.* **2018**, *165*, A2801.
[6] A. Sharafi, E. Kazyak, A. L. Davis, S. Yu, T. Thompson, D. J. Siegel, N. P. Dasgupta, J. Sakamoto, *Chem. Mater.* **2017**, *29*, 7961.
[7] R. Murugan, V. Thangadurai, W. Weppner, *Angew. Chem., Int. Ed.* **2007**, *46*, 7778.
[8] V. Thangadurai, S. Narayanan, D. Pinzaru, *Chem. Soc. Rev.* **2014**, *43*, 4714.
[9] C.-L. Tsai, V. Roddatis, C. V. Chandran, Q. Ma, S. Uhlenbruck, M. Bram, P. Heitjans, O. Guillon, *ACS Appl. Mater. Interfaces* **2016**, *8*, 10617.
[10] W. Luo, Y. Gong, Y. Zhu, Y. Li, Y. Yao, Y. Zhang, K. K. Fu, G. Pastel, C.-F. Lin, Y. Mo, E. D. Wachsman, L. Hu, *Adv. Mater.* **2017**, *29*, 1606042.
[11] T. Krauskopf, H. Hartmann, W. G. Zeier, J. Janek, *ACS Appl. Mater. Interfaces* **2019**, *11*, 14463.
[12] M. J. Wang, R. Choudhury, J. Sakamoto, *Joule* **2019**, *3*, 2165.
[13] P. Albertus, S. Babinec, S. Litzelman, A. Newman, *Nat. Energy* **2018**, *3*, 16.
[14] C.-H. Dustmann, *J. Power Sources* **2004**, *127*, 85.
[15] J. L. Sudworth, *J. Power Sources* **2001**, *100*, 149.
[16] J. L. Sudworth, *J. Power Sources* **1984**, *11*, 143.
[17] J. Kasemchainan, S. Zekoll, D. Spencer Jolly, Z. Ning, G. O. Hartley, J. Marrow, P. G. Bruce, *Nat. Mater.* **2019**, *18*, 1105.
[18] J. T. Kloprogge, L. V. Duong, B. J. Wood, R. L. Frost, *J. Colloid Interface Sci.* **2006**, *296*, 572.
[19] J. Zähr, S. Oswald, M. Türpe, H. J. Ullrich, U. Füssel, *Vacuum* **2012**, *86*, 1216.
[20] S. Hüfner, *Photoelectron Spectroscopy*, Springer, Berlin **2003**.
[21] A. Sharafi, H. M. Meyer, J. Nanda, J. Wolfenstine, J. Sakamoto, *J. Power Sources* **2016**, *302*, 135.
[22] M. Wang, J. B. Wolfenstine, J. Sakamoto, *Electrochim. Acta* **2019**, *296*, 842.
[23] G. T. Hitz, D. W. McOwen, L. Zhang, Z. Ma, Z. Fu, Y. Wen, Y. Gong, J. Dai, T. R. Hamann, L. Hu, E. D. Wachsman, *Mater. Today* **2019**, *22*, 50.
[24] L. Viswanathan, A. V. Virkar, *J. Mater. Sci.* **1982**, *17*, 753.
[25] L. C. De Jonghe, L. Feldman, A. Buechele, *Solid State Ionics* **1981**, *5*, 267.
[26] F. Han, A. S. Westover, J. Yue, X. Fan, F. Wang, M. Chi, D. N. Leonard, N. J. Dudney, H. Wang, C. Wang, *Nat. Energy* **2019**, *4*, 187.
[27] M. Fritz, M. Barbosa, G. Staikov, W. Lorenz, M. Steinbruck, R. Knodler, *Solid State Ionics* **1993**, *62*, 273.
[28] M.-C. Bay, M. V. F. Heinz, R. Figi, C. Schreiner, D. Basso, N. Zanon, U. F. Vogt, C. Battaglia, *ACS Appl. Energy Mater.* **2019**, *2*, 687.
[29] N. H. Nachtrieb, E. Catalano, J. A. Weil, *J. Chem. Phys.* **1952**, *20*, 1185.
[30] T. R. Jow, *J. Electrochem. Soc.* **1983**, *130*, 737.
[31] R. Furuya, N. Tachikawa, K. Yoshii, Y. Katayama, T. Miura, *J. Electrochem. Soc.* **2015**, *162*, H634.
[32] J. B. Bates, N. J. Dudney, B. Neudecker, A. Ueda, C. D. Evans, *Solid State Ionics* **2000**, *135*, 33.

© 2019 The Authors. Published by WILEY-VCH Verlag GmbH & Co. KGaA, Weinheim